Article

Unraveling the Photoluminescence Properties of the $Sr_{10}V_6O_{25}$ Structure through Experimental and Theoretical Analyses

Mayara Mondego Teixeira,* Amanda Fernandes Gouveia,* Alexsandro Gama de Sousa, Luís Fernando da Silva, Regiane Cristina de Oliveira, Miguel A. San-Miguel, Máximo Siu Li, and Elson Longo*

Read Online

ACCESS | Metrics & More | Article Recommendations | Supporting Information

ABSTRACT: White light photoluminescent materials can overcome many problems due to an intrinsic color balance, in addition to reducing the cost for application in emitting components and electronic devices. In this sense, to observe this phenomenon of photoluminescence, variations in the synthesis time at low temperatures were carried out, which also influenced the degree of structural order/disorder of strontium vanadate ($Sr_{10}V_6O_{25}$, SVO). The microwave-assisted hydrothermal route allowed us to evaluate the structural and morphological evolution of the SVO compound. Furthermore, this paper discusses how van der Waals forces influence the morphological evolution of a semiconductor as a function of orientation, induction, and dispersion interactions. The experimental study combined with theoretical approaches provided information about the structure and electronic properties of SVO. From the experimental data and theoretical analysis, we propose, for the first time, that the unit cell of the SVO structure is composed of three distorted $[SrO_x]$ (x = 6, 7, and 9) and two distorted $[VO_4]$ clusters. Photoluminescence measurements revealed an efficient broadband emission, and the conversion of ultraviolet light excitation into visible light was observed. The emission chromaticity showed that the structural disorders of the $[SrO_x]$ and $[VO_4]$ clusters present the possibility of change in the Commission Internationale de l'Éclairage emission color.
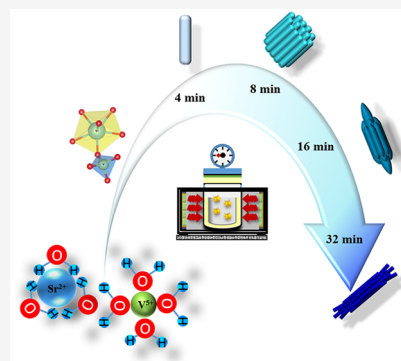
1. INTRODUCTION

After the appearance of commercial white light, the search for new color-converting phosphors such as white-light-emitting diodes (WLEDs) has been the focus of considerable research. WLED semiconductors have an advantage in lighting technology because they present high efficiency, low power consumption, good stability, adjustable colors, and lower risks of environmental damage.[1−3] Therefore, there is a tendency toward the substitution of conventional lamps by WLED devices.

The white light can be obtained by the combination of the red, green, and blue LED chips or by combining the blue LED chip and yellow phosphor or even using a near-ultraviolet (NUV) chip and red/green/blue tricolor conversion phosphors.[4−6] Indeed, several studies have been performed using blue, green, red, and yellow phosphors exhibiting high efficiency, chemical stability, and low cost.[2,5] However, the modulation of each phosphor color for the reproduction of WLEDs becomes the main challenge due to the low luminescence efficiency related to the strong reabsorption of the blue light by the red and green phosphors.[1,7] In this way, single-component white-light phosphors exhibiting luminous efficacy as well as a good color rendering index have been proposed to overcome the complications associated with the multiple emitting phosphors.[1,7] According to the literature, an efficient way to do that is

by using phosphors that convert the ultraviolet excitation radiation into broadband emission covering the whole visible light region, as this would reduce the types of phosphors used in LEDs as well as the production costs.[4]

The vanadate family has been considered promising for LEDs since they present a broadband emission covering almost the entire visible light region, high luminescence efficiencies, and excellent chemical stabilities.[5,8−12] In past years, different vanadate structures have been investigated, motivated by their luminescence properties.[11,13,14] Given that the vanadates exhibit the self-activated emitting properties of the VO_4^{3-} group, they can effectively convert UV radiation into visible light.[4,5] The luminescence mechanism of vanadium materials has been justified by the charge transfer in the VO_4^{3-} group from the 2p orbital of O^{2-} to the 3d orbital of V^{5+}.[12,14,15] The photoluminescence (PL) of the vanadium compounds is strongly dependent on the deformation degree of the VO_4 tetrahedron, which is influenced by the types and amounts of cations that are
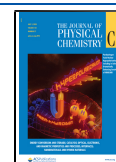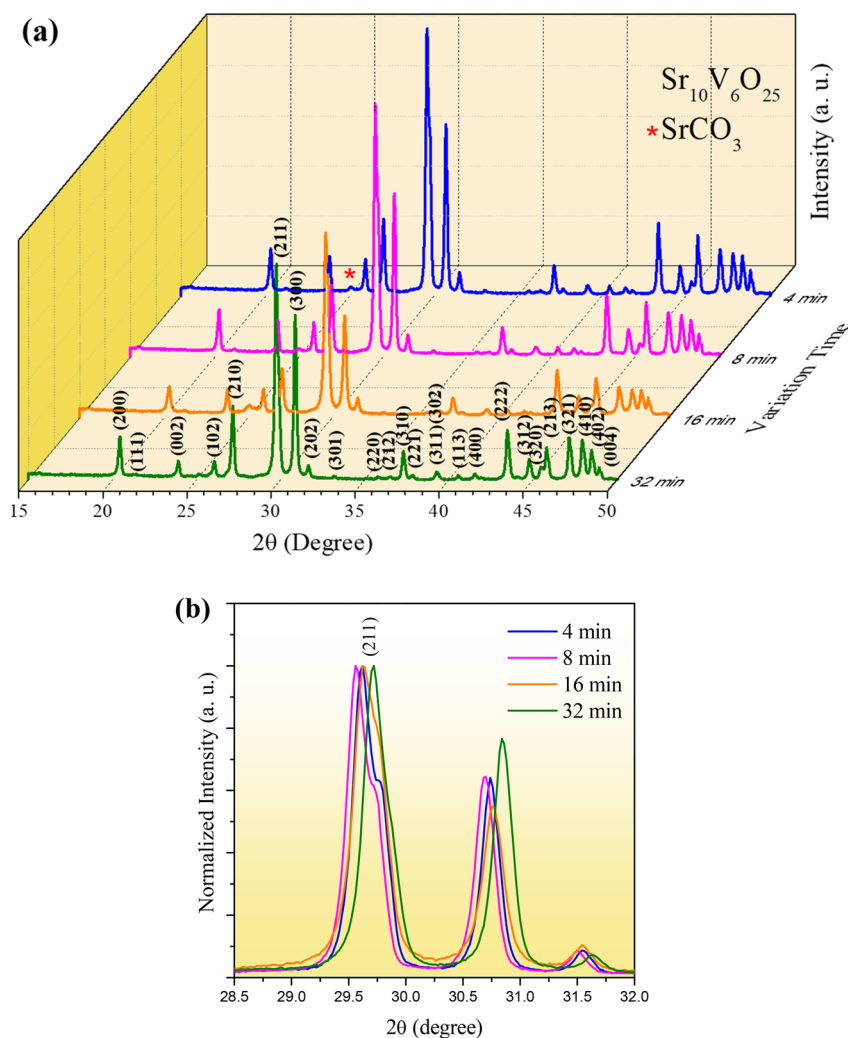
Figure 1. (a) XRD patterns of the $Sr_{10}V_6O_{25}$ samples with standard JCPDS No. 52-1578. (b) The normalized intensity of the (211) plane.

around the structure[4,16] since the $(^3T_1, ^3T_2 \rightarrow {}^1A_1)$ forbidden transitions by the spin selection rule in the ideal T_d symmetry become partially permitted by the spin−orbit interaction due to distortions in the VO_4 tetrahedron.[13,14] Different photoluminescent emissions have been obtained by substituting the network-modifying cation and also by structural lattice changes.[17]

Strontium vanadate compounds are promising for use as light-emitting phosphors, and some structures have already been elucidated regarding the PL property, such as $Sr_2V_2O_7$,[9,18] $Sr_3V_2O_8$,[19,20] and $Sr_6V_2O_{11}$.[15] The optical properties of the $Sr_{10}V_6O_{25}$ structure have not yet been reported and are the subject of this paper. For this purpose, $Sr_{10}V_6O_{25}$ samples were synthesized using a microwave-assisted hydrothermal (MAH) system at 120 °C and with short synthesis times. The samples were characterized by X-ray diffraction (XRD), field emission scanning electron microscopy (FE-SEM), and Raman and X-ray absorption near-edge structure (XANES) spectroscopies. The crystal growth and morphology, the phase formation, the photoluminescence excitation (PLE), and photoluminescence (PL) spectra were also investigated. To corroborate the experimental results, density functional theory (DFT) calculations were performed to study the $Sr_{10}V_6O_{25}$ structure and its electronic properties. This paper reports an experimental and theoretical investigation of the effects of the MAH time on the structural order/disorder degree and PL properties of the SVO compound.

2. MATERIALS AND METHODS

2.1. Synthesis of $Sr_{10}V_6O_{25}$ Powders. For the synthesis of $Sr_{10}V_6O_{25}$ powders, we started by dissolving 3 mmol of $Sr(NO_3)_2$ (Sigma-Aldrich, 99+%) and 1 mmol of Na_3VO_4 (Sigma-Aldrich, 99.98%) in 25 mL of deionized water, separately. The solutions were then mixed at room temperature, and a precipitate was formed. The pH was adjusted to 12.50 with 6 mol L^{-1} of KOH aqueous solution, and the final volume was adjusted to 70 mL. The precipitate was stirred for 1 h at room temperature. Then, the product was transferred to a Teflon autoclave, which was sealed and placed in the MAH system at 120 °C for 4, 8, 16, and 32 min. The samples were labeled according to the MAH synthesis time used, i.e., SVO_4, SVO_8, SVO_16, and SVO_32. The product formed was collected at room temperature and washed with distilled water to neutralize the pH (∼7). The powder samples were then dried in a conventional furnace at 60 °C for 24 h.

2.2. Characterization. XRD analyses were carried out with the Dmax-2500PC diffractometer, Rigaku/Japan, the source of Cu Kα radiation (λ = 1.5406 Å) in the 2θ range of 15°−50° at a step scan rate of 1°/min and step size of 0.02°. FE-SEM analyses were performed using an FEI microscope, Inspect F50, operated
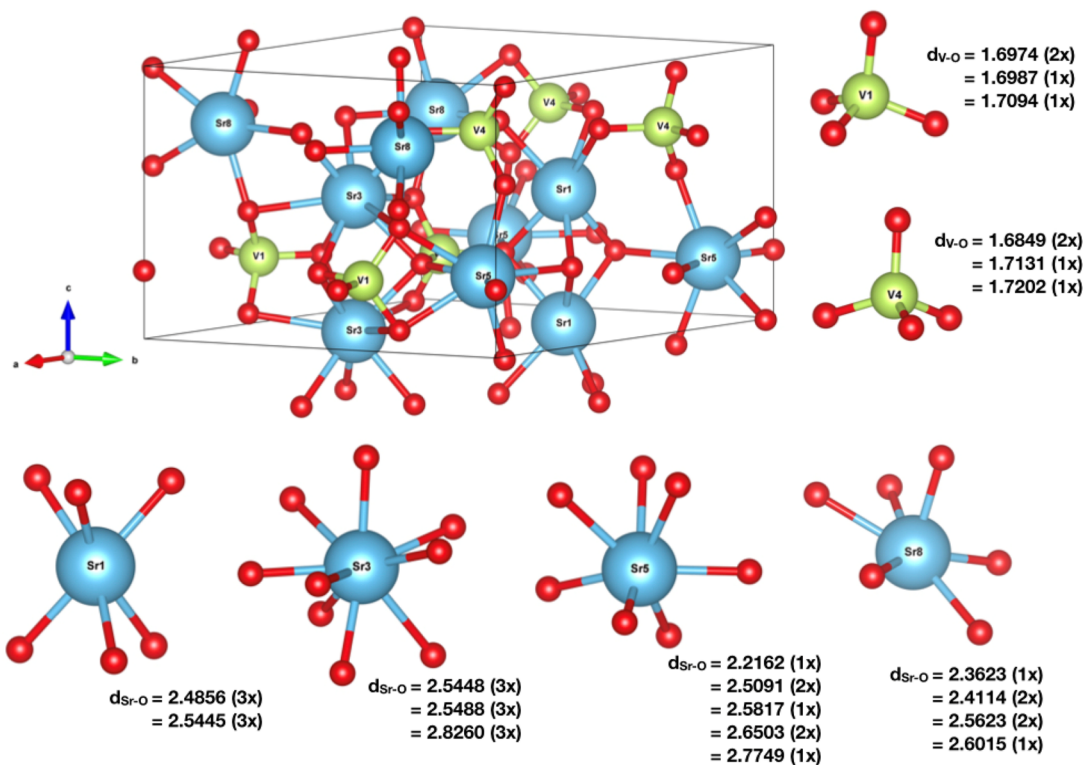
Figure 2. Hexagonal unit cell representation of $Sr_{10}V_6O_{25}$ and the bond length values of V−O and Sr−O in $[VO_4]$ and $[SrO_x]$ (x = 6, 7, and 9), respectively. The Sr, V, and O atoms are represented in blue, green, and red, respectively.

at 10 kV. FTIR spectra were collected at room temperature using a spectrophotometer (Equinox 55, Bruker) with a diffuse reflectance accessory. The spectra were collected at a resolution of 4 cm^{-1}, over wavenumbers ranging from 500 to 2000 cm^{-1}. XPS analyses were performed using the Scienta Omicron ESCA spectrometer, Germany, with monochromatic Al Kα (1486.7 eV). All of the binding energies were calibrated regarding the C 1s peak at 284.5 eV. The Raman spectra were taken via a Bruker Optics Senterra spectrometer employing a laser emitting at 532 nm settled to provide a laser power at the sample of about 5 mW. Measurements were collected across one spectral window from 50 to 1200 cm^{-1} at a spectral resolution of 3.5 cm^{-1}. X-ray absorption spectroscopy measurements were performed at the XAFS2 beamline on the Brazilian Synchrotron Light Laboratory (LNLS) which was operated at 1.36 GeV and 100−160 mA. XANES spectra of SVO samples were collected at the V K-edge (4966 eV) in a transmission mode at room temperature in the range 5460−5520 eV, using a Si(111) double-crystal monochromator. For comparison purposes among the different samples, all spectra were background removed and normalized using the first EXAFS oscillation as unity. The XANES spectra were analyzed using the MAX software.[21] The PL spectroscopy at room temperature was conducted by using the Thermal Jarrell Ash Monospec 27 cm monochromator, USA, coupled to a visible detector Hamamatsu R955 photomultiplier, Japan. A Coherent Innova 200 K Krypton ion laser (λ_{exc} = 350 nm), USA, was used as the excitation source with an incident power of ∼14 mW on the samples. The excitation and emission measurements were performed using a Fluorolog 3 FL3-122 fluorescence spectrophotometer, Horiba Jobin Yvon, equipped with a 450 W xenon lamp as the excitation source and a UV−vis photomultiplier detector R928P.

2.3. Model System and Computational Method. First-principles calculations were conducted inside the framework of density functional theory (DFT) using the CRYSTAL14 software package[22] associated with the B3LYP hybrid functional.[23,24] Diagonalization of the Fock matrix was performed at an adequate k-point grid (Pack−Monkhorst 1976) in the reciprocal space. The level of accuracy of the calculation of the Coulomb and exchange series was controlled by five parameters. The 10^{-8}, 10^{-8}, 10^{-8}, 10^{-8}, and 10^{-16} parameters were chosen for the Coulomb overlap, Coulomb penetration, exchange overlap, the first exchange pseudo-overlap, and second exchange pseudo-overlap, respectively, whereas the percentage of Fock/Kohn−Sham matrices mixing was set to 40. The integration in the reciprocal space was performed by sampling the Brillouin zone with a 4 × 4 × 4 Monkhorst−Pack mesh. Sr, V, and O atoms centers are described by basis sets: PS-311(1d)G, 86-411d4G, and 6-31d1, respectively, taken from the Crystal Web site.

The SVO material, with a hexagonal structure, presents two different lattice parameters "a" and "c" and seven irreducible atoms in the conventional cell with one-unit formula per unit cell (Z = 1). The theoretical calculation of this structure started from the XRD data results, and it was necessary to use the same strategy applied by us[25] on the $Ca_{10}V_6O_{25}$ calculations: remove one O atom of the structure through the ATOMREMO keyword of the CRYSTAL program to guarantee the system to be stoichiometric. From this point, full optimization of the $Sr_{10}V_6O_{25}$ was carried out. From the calculations using the numerical second derivatives of the total energies implemented in the CRYSTAL code, the Raman vibrational modes and their corresponding frequencies were obtained. The band structure of the $Sr_{10}V_6O_{25}$ was calculated for 200 k-points along the

appropriate high-symmetry paths of the correct Brillouin zone and also the density of states (DOS).

3. RESULTS AND DISCUSSION

The X-ray diffraction technique was used to determine the obtained crystalline phase and the long-range order/disorder in the samples' lattice. Figure 1a shows the XRD peaks corresponding to $Sr_{10}V_6O_{25}$ with a hexagonal structure and spatial group $P6_3/m$, in good accordance with the Joint Committee on Powder Diffraction Standards (JCPDS) file No. 52-1578. Although the XRD results show a small amount of $SrCO_3$, the MAH method is effective for obtaining SVO at a relatively low temperature (120 °C) and short synthesis time (4 min). The synthesis conditions are favorable for the formation of the $SrCO_3$ phase, which is easily obtained at room temperature.[26] All samples presented an XRD peak related to the $SrCO_3$ phase, according to JCPDS file No. 05-0418.[27]

To observe the long-range order/disorder effect of the SVO samples synthesized by the MAH method, the calculation of the full width at half-maximum (fwhm) value for the high-intensity diffraction plane (211) was performed (Figure 1b). The fwhm values were 0.30, 0.30, 0.31, and 0.26, for SVO_4, SVO_8, SVO_16, and SVO_32, respectively. Increasing the synthesis time to 32 min leads to a more ordered sample in the long range, with a lower fwhm value. Figure 1b also shows a lower shift of the diffraction peaks to high angle values, suggesting a contraction of the unit cell of the SVO_32 sample according to the Bragg equation, $\sin \theta = n\lambda/2d$. Moreover, the bond distance and bond angles of the interatomic interaction between V and O atoms in the network-forming $[VO_4]$ clusters were extracted using the VESTA program (version 3.3.9) (see Table SI-1). The comparison between all samples showed different V−O bond lengths and different O−V−O bond angles, indicating that these $[VO_4]$ clusters are highly distorted.

Figure 2 shows the representation of the SVO unit cell, illustrating a single conventional unit cell. The lattice parameters and atomic positions were confirmed using Rietveld refinement and were the starting point for the DFT calculations. Therefore, the model of the unit cell and the length of the bond in each cluster in Figure 2 are the results of the optimization of the theoretical calculations. The hexagonal unit cell of $Sr_{10}V_6O_{25}$ is composed of two and four different atoms of vanadium and strontium, respectively. The vanadium atoms, designated V1 and V4, are coordinated to four oxygen atoms with different bond lengths, forming two kinds of distorted tetrahedron $[VO_4]$ configurations, while the strontium atoms are coordinated to six, seven, and nine oxygen atoms, resulting in the formation of $[SrO_6]$, $[SrO_7]$, and $[SrO_9]$ configurations, respectively.

The FE-SEM micrograph shows the morphological behavior of the obtained SVO samples (Figure 3). It is possible to see that the crystal morphology was strongly influenced by the interaction time with the microwave irradiation in the MAH system. For the SVO_4 sample, the formation of particles with a morphology similar to self-organized spherical architectures with a mean diameter of 2.74 μm ($\pm$1.09) was observed (Figure 3a). The spherical organization is composed of a high number of aligned nanostems (Figure 3b). For the SVO_8 sample, the morphology remained similar to a spherical architecture with a mean diameter of 3.03 μm ($\pm$1.04) (Figure 3c and 3d). Furthermore, for the MAH times of 4 (SVO_4 sample) and 8 min (SVO_8 sample), particles with a stem-shaped morphology are formed by the oriented growth of the nanostems that are initially obtained. Thus, a morphological variation can be seen
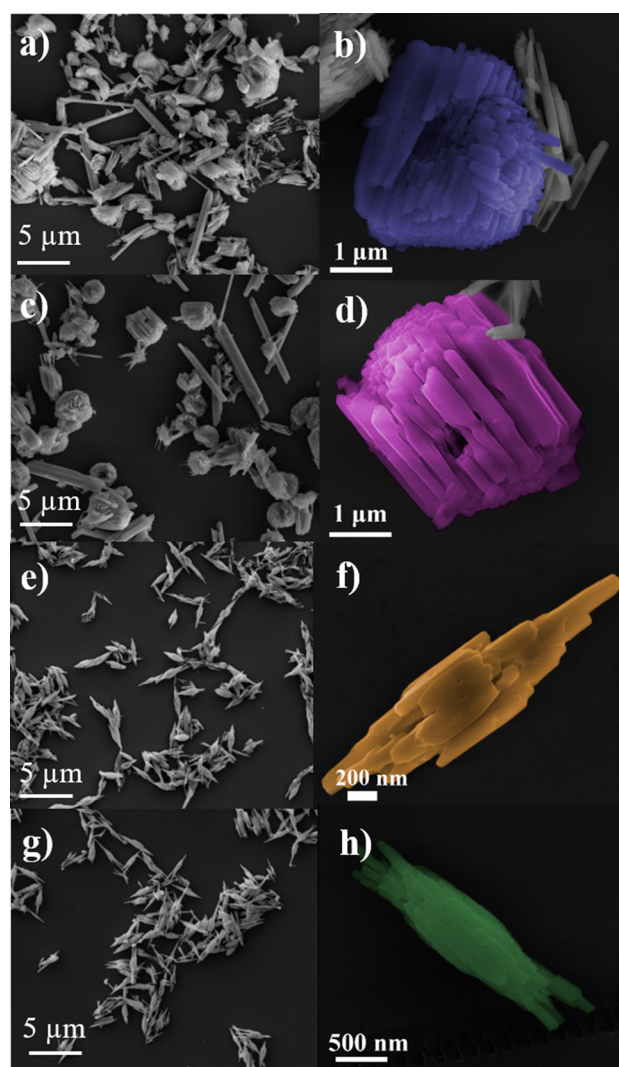

Figure 3. Low- and high-magnification FE-SEM images and size distribution histograms of $Sr_{10}V_6O_{25}$ samples obtained by the MAH method: (a,b) SVO_4, (c,d) SVO_8, (e,f) SVO_16, and (g,h) SVO_32.

between the particles. As the crystal growth time increased to 16 min in the MAH system (SVO_16 sample), the nucleation−dissolution−recrystallization process, effected by the microwave irradiation, caused the decomposition of the spherical morphologies into nanorods. The nanorods are bonded through coalescence, which produces particles with a mean diameter of 0.658 μm ($\pm$0.107) (Figure 3e and 3f). For a synthesis time of 32 min (SVO_32 sample), the particles had a mean diameter of 0.542 μm ($\pm$0.085), being formed by many nanorods (Figure 3g and 3h). These nanorods are possibly formed by the redissolution and recrystallization processes or by the splitting mechanism of rods that were formed earlier. The samples synthesized with synthesis times of 16 and 32 min presented a decrease in particle size in comparison with the samples obtained with shorter synthesis times (4 and 8 min). The action of the microwave irradiation increases the collision rate between the ions and also the particle nucleation process. Thus, it was possible to obtain well-organized particles in a short time and a morphological variation of the particles according to the synthesis time.
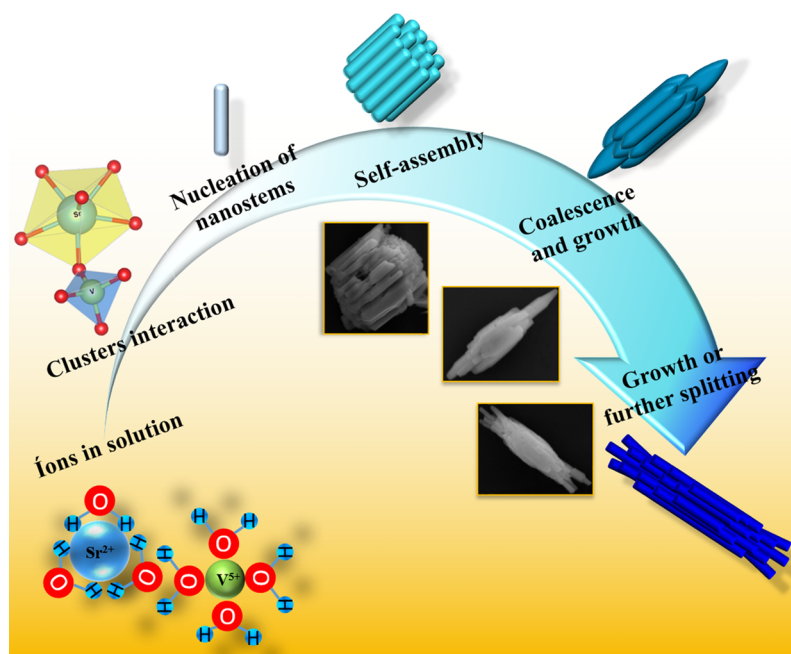
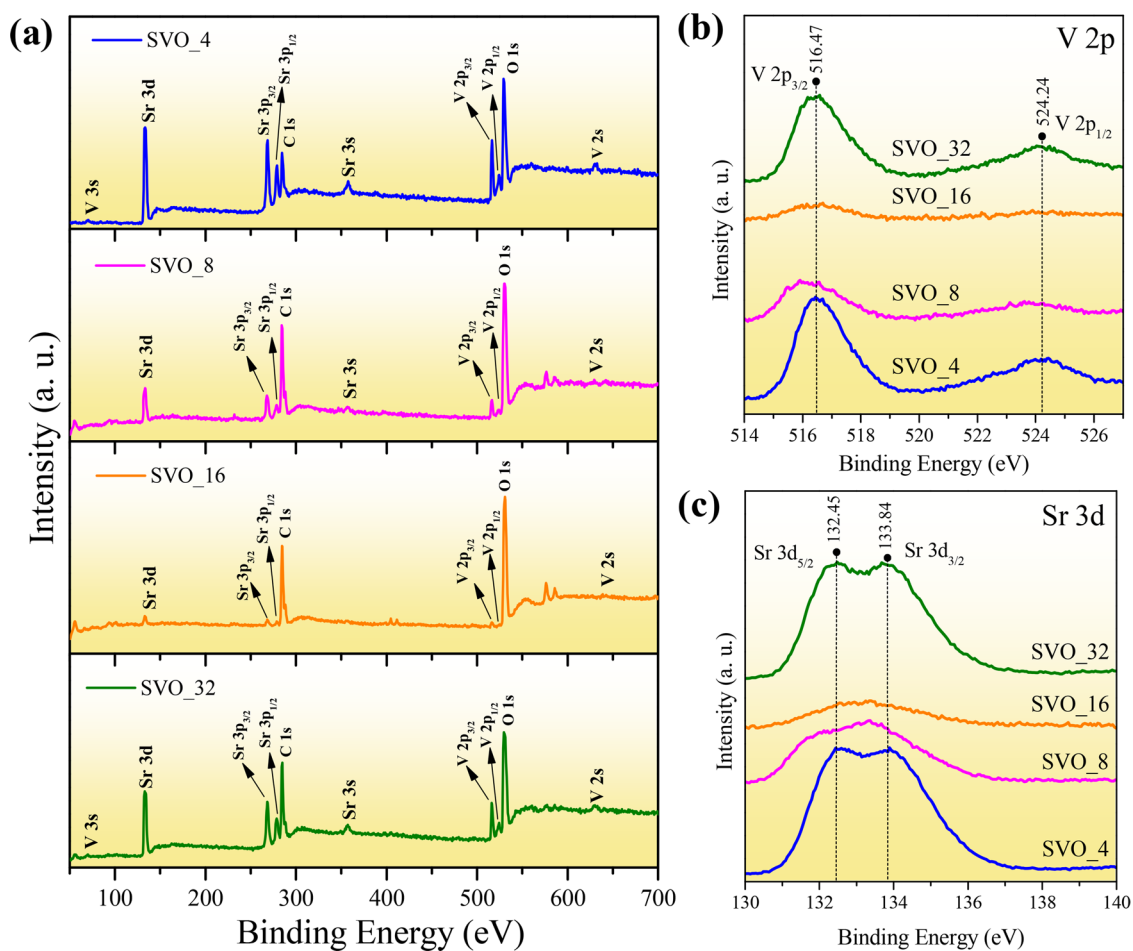**Figure 4.** Particle formation and growth scheme for $Sr_{10}V_6O_{25}$ with MAH synthesis time.

Figure 5. XPS spectra of the $Sr_{10}V_6O_{25}$ samples obtained by the MAH method at 120 °C with variation in synthesis time: (a) survey spectra, (b) V 2p, and (c) Sr 3d.

A scheme of particle formation and growth is shown in Figure 4. The solubilization of the precursors allows the availability of the Sr^{2+} and V^{5+} ions in solution. The microwave heating causes the collisions of the ions and consequently the formation of the
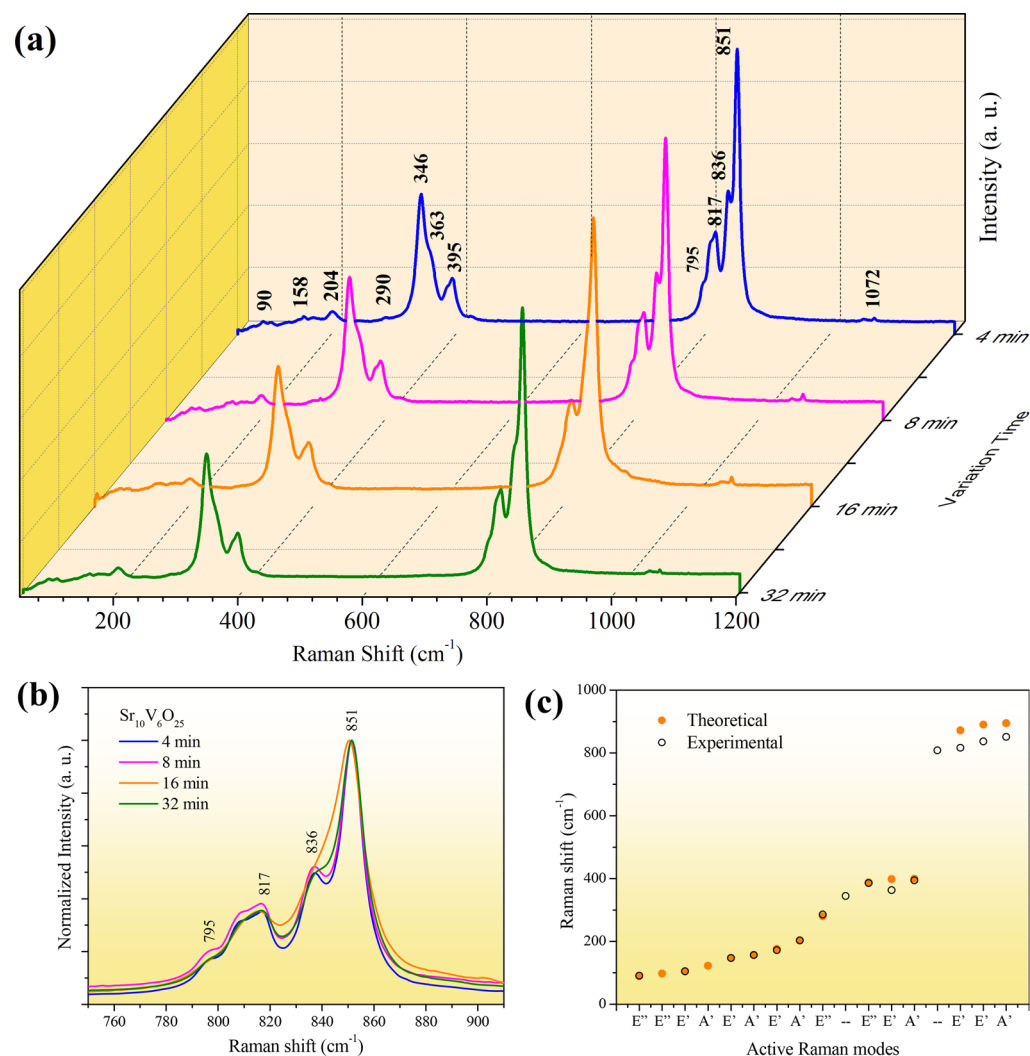
Figure 6. (a) Raman spectra of the $Sr_{10}V_6O_{25}$ samples obtained by the MAH method at 120 °C with variations in the synthesis time. (b) Normalized intensity of the 852 cm^{-1} peaks. (c) Comparison between relative Raman positions of experimental and theoretical results.

$[SrO_x]$ and $[VO_4]$ clusters. Short distance interactions between V and Sr with O atoms dominate the formation of these clusters (intracluster interactions). The interaction between these clusters at the medium-range cooperate to form crystalline network moieties (intercluster interactions),[28] resulting in the SVO lattice periodically extended over a long distance.

Initially, the intracluster interactions between Sr−O within the $[SrO_x]$ clusters and V−O within the $[VO_4]$ clusters occur by induction, with the permanent moment of these clusters deforming the electronic density of the neighboring ones. In this way, in the network-forming $[VO_4]$ clusters and the network-modifying $[SrO_x]$ clusters, there are modifications in angles between the atoms and in the lengths of the chemical bonds (Table SI-1). The modifications in the $[SrO_x]$ clusters were observed through two clusters: $[SrO_6]$ cluster with trigonal prism arrangement and $[SrO_7]$ clusters. As a result, the distortions expand to the lattice in the medium range by orientation interactions, in which different $[VO_4]$–$[VO_4]$, $[VO_4]$–$[SrO_9]$, $[VO_4]$–$[SrO_7]$, $[VO_4]$–$[SrO_6]$, $[SrO_9]$–$[SrO_7]$, $[SrO_9]$–$[SrO_6]$, or $[SrO_7]$–$[SrO_6]$ complex clusters interact by the rotational motion of their permanent moments. As a consequence, the long-range dispersion interactions in the crystal lattice cause the polarization of some regions of the particle. As a result of these interactions, surfaces with different

surface energies are produced. These in turn direct the nucleation of the crystallites, forming particles with nanostem morphology that interact and aggregate to create a self-organized spherical particle. The variation in the MAH synthesis time causes the redissolution/recrystallization process that affects the intracluster and intercluster interactions, changing the exposed surfaces. Different exposed surfaces affect the collision and shock of the particles, consequently conditioning the final morphology.

Different interactions between $[SrO_x]$ (x = 6, 7, and 9) and $[VO_4]$ clusters cause the coalescence of the particles that turn into nanorod agglomerates. Subsequently, these rods may undergo a process that splits them into smaller rods. These rods then agglomerate or undergo a new stage of the redissolution and recrystallization process to form the morphology observed in the final synthesis time of 32 min. Therefore, the interaction between $[SrO_x]$ and $[VO_4]$ clusters causes a short-, medium-, and long-range order/disorder effect on the newly created excited states on different surfaces, and as a consequence, there is a change in particle morphology that results in different PL properties.

The FTIR (Figure SI-1 of the Supporting Information (SI)) and the XPS (Figure 5) measurements were performed to investigate the presence of the $SrCO_3$ phase that is together with
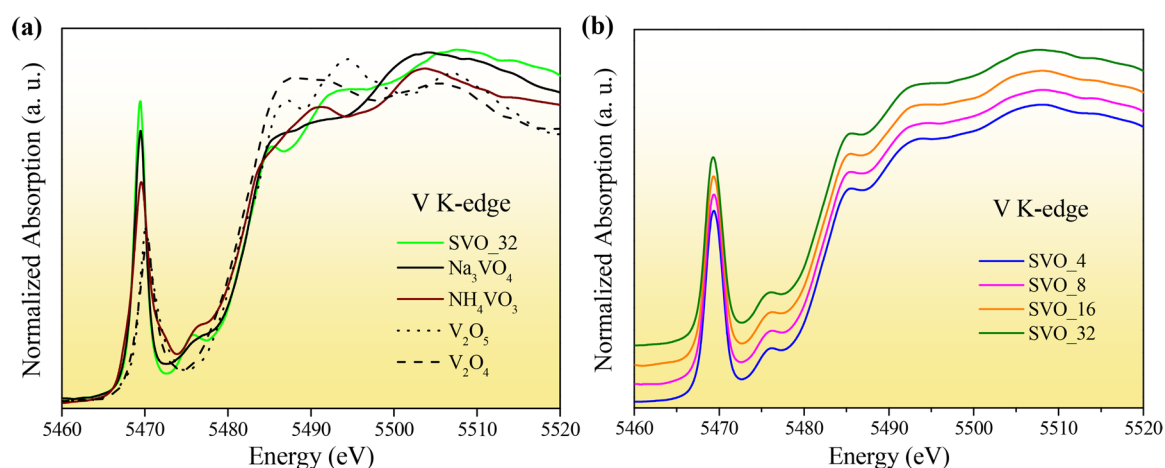
Figure 7. (a) Normalized XANES spectra of reference compounds and the SVO_32 sample. (b) Normalized V K-edge XANES spectra of the $Sr_{10}V_6O_{25}$ samples obtained by the MAH method at 120 °C with variations in synthesis time.

SVO samples as was observed previously by XRD (Figure 1a). Figure SI-1 shows the FTIR spectra for the SVO samples. The band at 556 cm^{-1} is attributed to the angular deformation of the V−O−V bond.[29] The bands at 820 and 876 cm^{-1} are assigned to the asymmetric (ν_3) and symmetric stretching (ν_1) vibrations of the V−O bonds of the VO_4 tetrahedron.[30][31] The 967 cm^{-1} mode corresponds to symmetric stretching vibrations of the shorter V−O bond.[32] All samples presented bands around 1393 and 1426 cm^{-1} that are related to the elongation vibrations (ν_3) of CO_3 ions.[31] The strong and broad band at 1493 cm^{-1} is attributed to the asymmetric stretching vibration of the C−O bond.[33] Finally, the band at 1659 cm^{-1} corresponds to bending vibrations of adsorbed H_2O molecules.[29][30]

The survey spectra (Figure 5a) showed that all SVO samples presented peaks of Sr, V, O, and C atoms and indicate the formation of the $SrCO_3$ phase being confirmed by the high-resolution spectra of the C 1s and O 1s (Figure SI-2). In the deconvolution of the high-resolution spectrum of the C 1s, the presence of three peaks of binding energy (BE) was observed. The peak at ca. 284 eV (red) corresponds to carbon contamination from the atmosphere, while the peak at ca. 288 eV (purple) is related to the carbonate phase (O−C═O).[34] The deconvolution of O 1s spectra is shown in Figure SI-2b. The peak at ca. 529 eV (blue) is attributed to lattice oxygen ions (O^{2-}) within the SVO.[34][35][36] The peak at ca. 531 eV (pink peak) is related to O bonded with C (O−C) in the carbonate ions (CO_3^{2-}), which confirms the presence of $SrCO_3$.[26][34] The SVO_8 and SVO_16 samples presented a higher percentage of superficial carbonate at 47.70% and 53.31%, respectively, confirming the intense carbon peak in the survey (Figure 5a). The peak O 1s at ca. 532 eV (olive) may be related to the oxygen in C−O(H)[37] or chemisorbed oxygen impurities (CO_2, H_2O, or adsorbed O^{2-}).[38] High-resolution spectra of Sr 3d and V 2p are shown in Figure 5b and 5c. The higher BE of V ($2p_{3/2}$, $2p_{1/2}$) at 516.47 and 524.24 eV are attributed to the oxidation state V^{5+} (Figure 5b).[37] The Sr 3d high-resolution spectra show the characteristic splitting of the peak into two $3d_{5/2}$ and $3d_{3/2}$ spin−orbit doublets centered at 132.45 and 133.84 eV, respectively (Figure 5c).

The SVO_8 and SVO_16 samples exhibited a lower BE intensity of the V and Sr atoms. This can be related to the high-intensity C 1s peak, suggesting that there may be a high amount of $SrCO_3$ in these samples due to strong interaction with CO_2 and H_2O molecules[39][40][41][42] (Figure 5a). The amount of surface

carbonate interfered in the identification of Sr and V atoms in the structure of the samples, as can be seen in Figure 5b and 5c. Although there was carbonate on the surface of the samples, as detected in the XRD spectra (Figure 1), it does not have a strong influence on the properties of the crystals.

The Raman spectra for SVO samples synthesized with different synthesis times at 120 °C in the MAH system are shown in Figure 6a. Bands in the lower frequency region of 100−290 cm^{-1} are assigned to lattice mode vibrations. In the range of 346−852 cm^{-1}, bands are attributed to the VO_4^{3-} tetrahedron.[32][43] At 346 and 363 cm^{-1}, bands are assigned to O−V−O symmetric bending vibrations. At 395 cm^{-1} the band corresponds to bending vibrations. The shoulder at 795 cm^{-1} is attributed to O−V−O asymmetric stretching vibrations, while the 817, 836, and 851 cm^{-1} bands are attributed to V−O symmetric stretching vibrations. All samples presented the band at 1072 cm^{-1} with a lower intensity corresponding to the $SrCO_3$ phase.[44][45] These relative positions of the Raman-active modes obtained experimentally are compared with the theoretical results in Figure 6c. This comparison confirms the good agreement of both experimental and theoretical results.

The short-range order/disorder effect was studied using the fwhm calculation of the band at 851 cm^{-1}, corresponding to the [VO_4] cluster in the $Sr_{10}V_6O_{25}$ structure (Figure 6b). The fwhm values found were 10.07, 12.64, 21.26, and 16.67 for the samples SVO_4, SVO_8, SVO_16, and SVO_32, respectively. The SVO_4 and SVO_8 samples obtained with the short synthesis times of 4 and 8 min at 120 °C showed lower values of fwhm and definition in the bands (Figure 6b). This indicates a possible short-range order. Increasing the synthesis time to 16 min resulted in the redissolution/recrystallization process of the particles, as indicated by the change in the morphology of the particles (Figure 3f) and by the increase of the short-range disorder in this material. For a synthesis time of 32 min, the particles begin to reorganize, leading to a slight decrease in the fwhm value observed for the SVO_32 sample.

XANES spectroscopy is a powerful technique to probe the local structure of amorphous and crystalline materials. Figure 7a shows the V K-edge XANES spectrum of the representative sample SVO_32 and also the vanadium-based reference compounds, i.e., Na_3VO_4, NH_4VO_3, V_2O_4, and V_2O_5. It can be seen that the spectrum of the SVO_32 sample is similar to the Na_3VO_4 reference spectrum, where the VO_4^{3-} orthovanadate group and the V cation are coordinated by four oxygen anions in

a tetrahedral symmetry (T_d) and with a V^{5+} oxidation state.[46] In addition, the pre-edge peak of the SVO_32 sample presents a prepeak slightly more intense when compared to the Na_3VO_4 reference peak, suggesting an increase in the degree of disorder in the $[VO_4]$ clusters.[47,48,49,50]

To observe the influence of the MAH synthesis time on the electronic structure and local order/disorder in $[VO_4]$ clusters, V K-edge XANES spectra were collected, as displayed in Figure 7b. The similarities between the spectra of the SVO samples indicate that vanadium is in a tetrahedral symmetry, with an oxidation state of 5+. Furthermore, it can be inferred that the pre-edge peak is characteristic of vanadium's tetrahedral coordination, originating from transitions from V 1s core levels to the 3d state. This transition is forbidden by the dipole selection rules in a centrosymmetric system but allowed in a noncentrosymmetric system occasioned by a strong mixture of the 3d and 4p orbitals and the overlapping of the 3d orbital with the 2p orbitals of the surrounding O atoms.[18,47,51,52] As mentioned above, the SVO samples exhibited local disorder around $[VO_4]$ clusters; however, the increase of MAH synthesis time did not affect the degree of disorder of the samples, as seen in Figure 7b.

To understand the electronic structure and the PL property of the SVO, the band structure (Figure 8) and the density of states
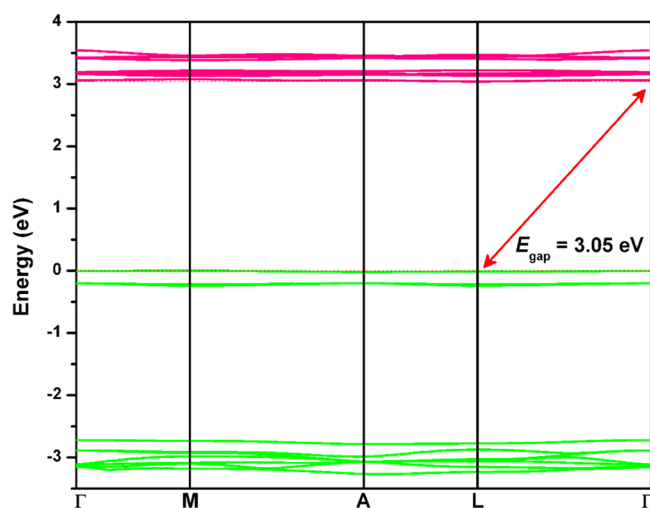

Figure 8. Band structure calculated for the $Sr_{10}V_6O_{25}$ structure with an indirect transition between the VB and CB.

(DOS, Figure 9) were analyzed from the theoretical calculations. The band structure reveals the values of the optical band gap energy (E_{gap}) involved in the electronic transitions between the valence band (VB) and the conduction band (CB) in a perfect SVO crystal. The calculated value of E_{gap} is 3.05 eV and is an indirect transition between the L−Γ points in the Brillouin zone. It is important to highlight that the direct transition between the Γ-points is very near the indirect value, with an E_{gap} value of 3.07 eV.

To verify what kind of orbitals are involved in these electronic transitions, it is necessary to analyze the DOS, which gives information about these atomic orbitals. From the analyses of the projected DOS on each atom (Figure 9a), it is possible to affirm that the VB is mainly composed of a major contribution of O atoms and a minor contribution of Sr atoms. It is also possible to conclude that the top of this band, in other words, the last occupied orbital of the VB, derives from the O $2p_z$ and Sr $4p_z$ +
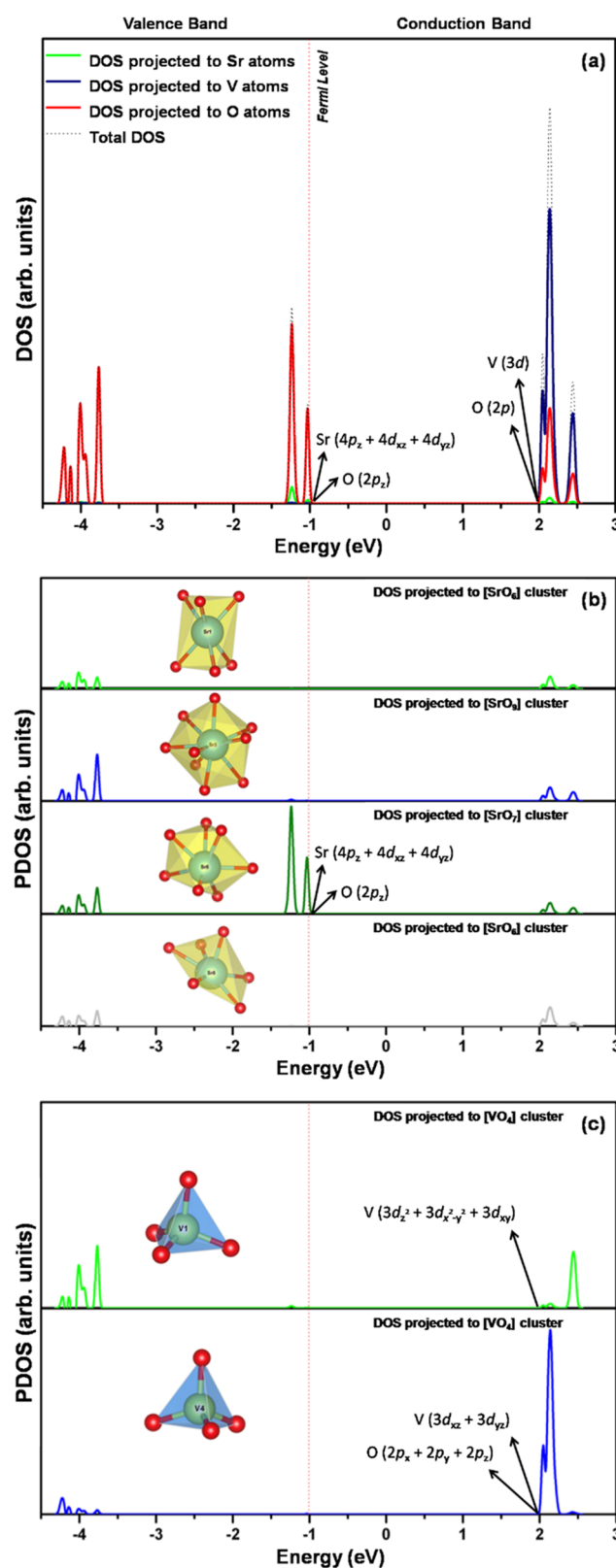

Figure 9. Density of states projected on the $Sr_{10}V_6O_{25}$ structure: (a) total atoms, (b) $[SrO_6]$, $[SrO_7]$, and $[SrO_9]$ clusters, and (c) $[VO_4]$ clusters.

$4d_{xz}$ + $4d_{yz}$ orbitals. In contrast, the CB is mainly formed by the V states, with a significant contribution of O states. The bottom of this band derives from the V 3d and O 2p orbitals. To understand how the $Sr_{10}V_6O_{25}$ structure is formed by a different
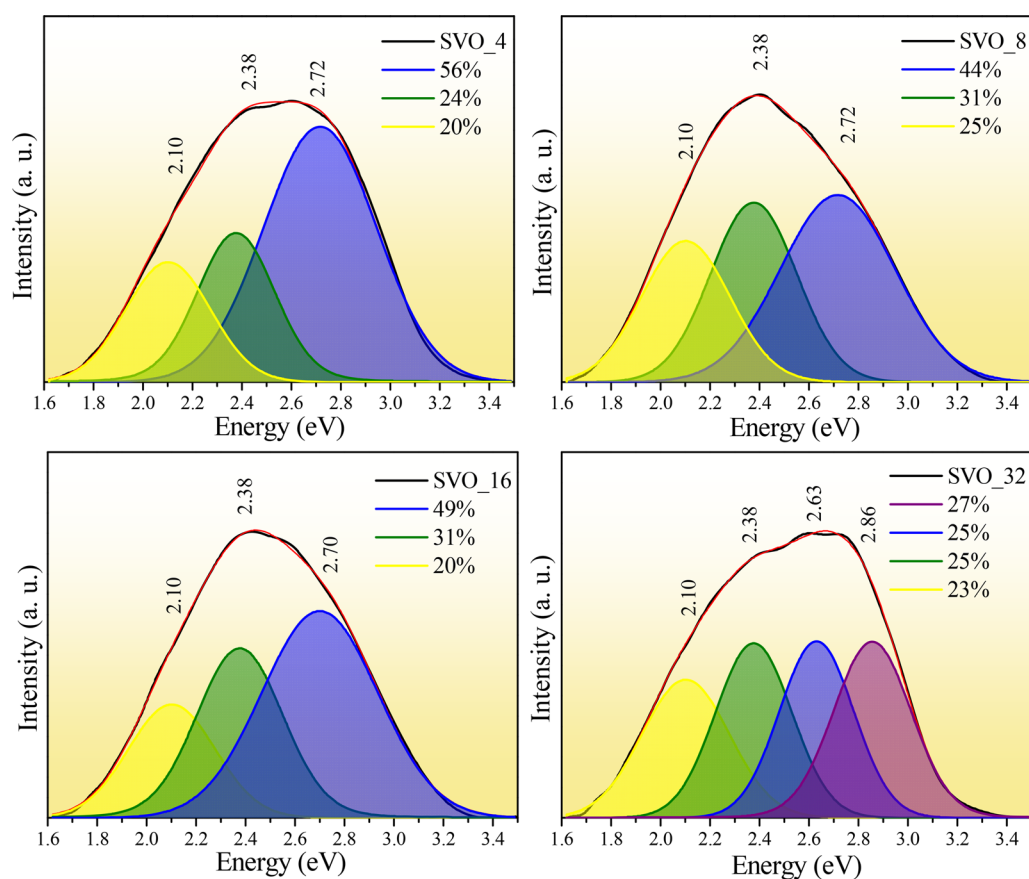
Figure 10. Deconvolution of PL spectra with Voigt Area G/L curves (red line) and percentage of color area in the violet, blue, green, and yellow regions for the $Sr_{10}V_6O_{25}$ samples obtained by the MAH method at 120 °C with synthesis time variation.

arrangement of V and Sr atoms, an analysis of the partial DOS (PDOS) from these different clusters was also performed. Figure 9b shows the PDOS derived from the $[SrO_6]$, $[SrO_7]$, and $[SrO_9]$ clusters. From this result, it is possible to affirm that the atomic orbitals of $[SrO_7]$ clusters are responsible for the last occupied orbital of the VB with the O $2p_z$ and Sr $4p_z$ + $4d_{xz}$ + $4d_{yz}$ orbitals. Figure 9c presents the PDOS derived from both $[VO_4]$ clusters. There are two different $[VO_4]$ clusters in the $Sr_{10}V_6O_{25}$ structure which are named by V1 and V4 atoms, and according to our result, it is possible to affirm that the atomic orbitals of V atoms from both $[VO_4]$ clusters are responsible for the first unoccupied orbital of the CB, comprising the V 3d ($3d_{z^2}$ + $3d_{xz}$ + $3d_{yz}$ + $3d_{x^2-y^2}$ + $3d_{xy}$), and only the O 2p orbitals coordinated to the V4 atoms contribute to this first unoccupied orbital at the bottom of the CB, as shown in Figure 9c. Thus, it can be proposed that the electronic transitions in the SVO occur from the excitation of the VB maxima region, located in the atomic orbitals corresponding to the Sr−O bond of the $[SrO_7]$ clusters, to the CB minimum region, corresponding to the empty atomic orbitals located at the V−O bond of the $[VO_4]$ clusters.

The PL properties of the SVO samples were monitored at room temperature with excitation at 350 nm (Figure 10). PL spectra were fitted with three Voigt Area G/L curves centered at 2.72 eV (blue region), 2.38 eV (green region), and 2.10 eV (yellow region) for SVO_4, SVO_8, and SVO_16 samples, respectively. The SVO_32 sample presents additional emissions at 2.86 eV (violet region) and 2.63 eV (blue region), showing a small shift of the emission for the high energy. The emission displacement refers to the difference in energy (ΔE) between the VB and CB, being related to the distortions in the V−O

bonds in the $[VO_4]$ clusters.[53] These distortions are related to the different forms of intracluster and intercluster interactions between $[SrO_x]$ and $[VO_4]$ clusters that change the degree of order/disorder in the crystal lattice.[28] As a result, the excited states of the different surfaces change, which in turn changes the band gap, the morphology, and consequently the PL. As observed in the XRD spectrum (Figure 1b), the SVO_32 sample showed a lattice contraction, and by decreasing the V−O distance, the transition energies ΔE increased, presenting high energy emission in the violet and blue regions.[13] Therefore, the long- and short-range structural distortions in the SVO samples lead to a change of the surface and energy levels and thus a change in the PL properties of the samples. In addition to the charge transfer transitions from the $[SrO_7]$ to $[VO_4]$ cluster, there is the contribution of additional energy levels within the band gap. In this way, it can be proposed that the distortions present in the $[VO_4]$ clusters have caused the formation of defects (intermediate levels between the VB and CB) that are responsible for the emissions in the green and yellow regions. In order to understand the PL mechanism observed in Figure 10, excitation and emission measurements were performed for all samples using a xenon lamp, as shown in Figure 11. In this way, the emission spectra were constructed with excitation at 350 nm, the same energy used in the laser excitation.

The excitation (PLE) and emission (PL) spectra for SVO samples prepared with different synthesis times at 120 °C are shown in Figure 11. The PLE spectrum was made by monitoring the maximum emission at 500 nm of the PL spectra shown in Figure SI-3a, which is the same maximum for the PL spectra of Figure 10. Figure 11a shows that all samples presented a
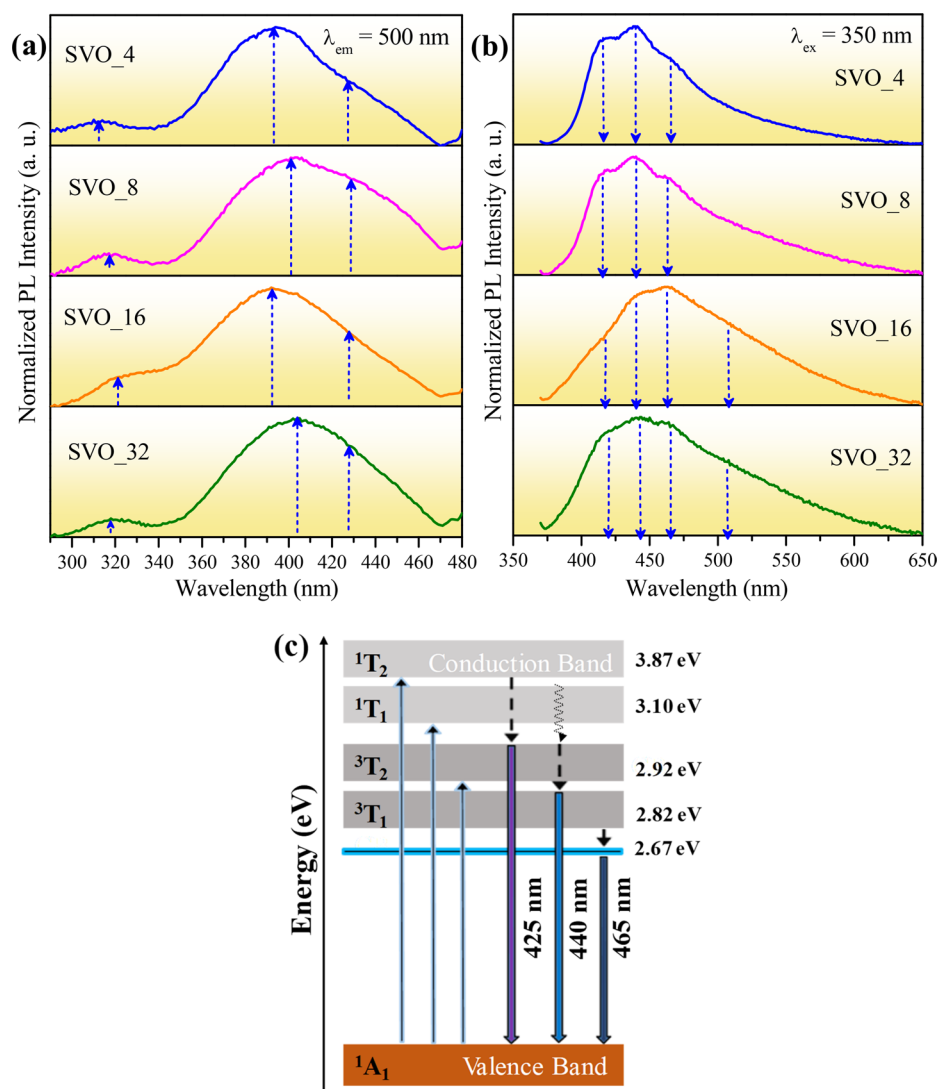
Figure 11. (a) PLE spectra (λ_{em} = 500 nm), (b) PL spectra (λ_{ex} = 350 nm), and (c) PL mechanism for the $Sr_{10}V_6O_{25}$ samples obtained by the MAH method at 120 °C with synthesis time variation.

broadband excitation from 300 to 470 nm with a maximum near 400 nm (3.10 eV) and a weaker band near 320 nm (3.87 eV). For the PL spectra, the samples were excited at 350 nm, and the same energy was used for the PL spectra of Figure SI-3a. All samples show a broadband emission from 375 to 650 nm, with a maximum near 440 nm (2.82 eV) (see Figure 11b). These transitions are attributed to ligand−metal charge transfers in the tetrahedral $[VO_4]$ cluster with T_d symmetry.[13,15,54] Given these results, a PL mechanism was proposed for the $Sr_{10}V_6O_{25}$ structure.

The PL mechanism for SVO samples is shown in Figure 11c. First, the electronic excitation process occurs from the ground state $^1A_1$ to the excited states $^1T_2$ and $^1T_1$. Then, a decay to lower energy levels, $^3T_2$ and $^3T_1$, occurs, and only then the electron decays to the ground state ($^1A_1$) with photon emissions. In the PLE spectra, the absorption occurs at 320 nm (3.87 eV), corresponding to the charge transfer transition $^1A_1 \rightarrow {}^1T_2$ and the high transition intensity at ~400 nm (3.10 eV), corresponding to the $^1A_1 \rightarrow {}^1T_1$ absorption. The maximum intensity absorption is attributed to the charge transfer transition from the O 2p orbital, with a small contribution from Sr 4p and 4d to the V 3d orbital. Besides, the broadband spectra of PLE

show that other energy states, such as $^3T_2$, may have been populated since an absorption at ~425 nm (2.92 eV) is observed for all the samples. The transitions ($^1A_1 \rightarrow {}^3T_2$) become partially possible due to the spin−orbit interaction originated by the distortions in the $[VO_4]$ clusters.[54,55] These distortions can be originated from interactions with the different distorted $[SrO_x]$ clusters that have participation in the VB.

The PL spectra show the emission bands at 425 nm (2.92 eV) for the $^3T_2 \rightarrow {}^1A_1$ transition and at 440 nm (2.82 eV) for the $^3T_1 \rightarrow {}^1A_1$ transition as well as emission at ~465 nm (2.67 eV), which was attributed to the energy level within the band gap and shallow defects in the blue region that are close to the CB (see Figure 11c). For the SVO_16 and SVO_32 samples, emission at 507 nm was observed, indicating the formation of a further intermediate state at 2.44 eV, which is formed due to the high short-range distortions in the $[VO_4]$ clusters, as seen in Figure 6b. The distortions cause a change in charge density around the V and Sr atoms and thus favor the formation of intermediate states within the band gap of the materials. Furthermore, all samples exhibited broadband emission from 350 to 650 nm, with displacements at the maximum emission. The difference in PL emissions is due to distortions in $[SrO_x]$ and $[VO_4]$ clusters

in the SVO lattice, which cause a change in the microstructure and surface energy of the samples.

To evaluate the difference in PL for all samples, the chromaticity coordinates (x, y) of the Commission Internationale de l'Éclairage (CIE) diagram were obtained (see Figure SI-3b and Table SI-2). The literature shows that the CIE coordinates for the balanced white light region are in the range x = 0.28 to 0.35 and y = 0.30 to 0.37.[56,57] Therefore, the SVO_32 sample has a PL emission close to the pure white point at x = 0.33 and y = 0.33 (see Table SI-2). The prolonged synthesis time (32 min) caused the dissolution and recrystallization process, which generated a contraction in the crystal lattice, resulting in large V−O distortions in the short range, as shown in the XRD and Raman spectra (Figure 1b and 6b). These distortions alter the surface energy and consequently change the band gap due to the formation of defects as intermediate levels in the forbidden region, which contributed to the emission (see Figure 10). The broadband emission for the SVO_32 sample favored PL in the white light region of the CIE chromaticity diagram. For the other samples, only three levels of emission energy were observed in the blue, green, and yellow regions (Figure 10). The SVO_4 sample showed a high percentage of blue emission (56%), in the cyan region of the CIE chromaticity diagram. The SVO_16 presented 49% of the blue emission, in the bluish-green region of the CIE color diagram, and the SVO_8 sample has a shift to the green region in the CIE color diagram. In this way, it can be observed that the variation in the synthesis time (4, 8, 16, and 32 min) in the MAH system caused different types of order/disorder in the lattice, which changed the surface energy, altering the band gap and the PL property of the SVO.

4. CONCLUSION

The $Sr_{10}V_6O_{25}$ structure was successfully obtained by the MAH system at a temperature of 120 °C and short times of 4, 8, 16, and 32 min. The diffractograms and micrographs showed that the microwave system favored the formation of the particle with a hexagonal structure with different morphologies. The variation in synthesis times modified the intracluster and intercluster interactions in the short-, medium-, and long-range and thus promoted a change in the surface energy, altering the morphology and particle size. Raman spectroscopy confirmed structural distortions in the $[VO_4]$ clusters of the network of samples obtained with longer synthesis times of 16 and 32 min. The variation in synthesis time in the microwave system caused different distortions in the SVO lattice, mainly in the $[VO_4]$ cluster. XANES spectra confirmed that all samples are formed by tetrahedral $[VO_4]$ clusters where V atoms have oxidation state +5. Theoretical calculations confirmed that the VB is composed of $[SrO_x]$ states, with a major contribution of $[SrO_7]$ clusters on the top of this band, and the CB is mainly composed of states from $[VO_4]$ clusters. They also confirmed that there is no significant difference between a direct and indirect electronic transition in the $Sr_{10}V_6O_{25}$ structure. The phosphors were excited by UV light centered at 350 nm at room temperature and showed a broadband emission from 350 to 750 nm with a maximum emission near 500 nm. The CIE chromaticity diagram showed emissions in the white region. The UV light from a 150 W xenon lamp allowed us to understand the process of excitation and emission within the SVO samples, and thus a PL mechanism was proposed for these samples. It can be concluded that distortions in the $[SrO_x]$ and $[VO_4]$ clusters create new intermediate levels within the band gap, possibly modifying the surface energy, morphology, and photoluminescent property of the samples.

■ ASSOCIATED CONTENT

ⓢ Supporting Information

The Supporting Information is available free of charge at https://pubs.acs.org/doi/10.1021/acs.jpcc.0c02768.

Bond distance and bond angles of the $[VO_4]$, $[SrO_6]$, and $[SrO_7]$ clusters. Fourier transform infrared spectra. High-resolution XPS spectra of C 1s and O 1s. Photoluminescence spectra at room temperature with λ_{ex} = 350 nm and CIE chromaticity diagram (PDF)

■ AUTHOR INFORMATION

Corresponding Authors

Elson Longo − CDMF-UFSCar, Universidade Federal de São Carlos, 13565-905 São Carlos, São Paulo, Brazil; ⓞ orcid.org/0000-0001-8062-7791; Email: elson.liec@gmail.com

Mayara Mondego Teixeira − CDMF-UFSCar, Universidade Federal de São Carlos, 13565-905 São Carlos, São Paulo, Brazil; ⓞ orcid.org/0000-0001-9038-0024; Email: mayaramondego.ufma@gmail.com

Amanda Fernandes Gouveia − Institute of Chemistry, State University of Campinas, 13083-970 Campinas, São Paulo, Brazil; ⓞ orcid.org/0000-0003-3441-3674; Email: amandafernandes.gouveia@gmail.com

Authors

Alexsandro Gama de Sousa − UESB, Universidade Estadual do Sudeste da Bahia, 45700-000 Bahia, Brazil

Luís Fernando da Silva − Departamento de Física, Universidade Federal de São Carlos, 13565-905 São Carlos, São Paulo, Brazil; ⓞ orcid.org/0000-0001-6257-5537

Regiane Cristina de Oliveira − Grupo de Modelagem e Simulações Moleculares, Universidade Estadual Paulista Júlio de Mesquita Filho, Faculdade de Ciências, 17033-360 Bauru, São Paulo, Brazil; ⓞ orcid.org/0000-0002-7332-8731

Miguel A. San-Miguel − Institute of Chemistry, State University of Campinas, 13083-970 Campinas, São Paulo, Brazil; ⓞ orcid.org/0000-0002-6650-7432

Máximo Siu Li − IFSC-Universidade de São Paulo, 13560-970 São Carlos, São Paulo, Brazil

Complete contact information is available at:
https://pubs.acs.org/10.1021/acs.jpcc.0c02768

Notes

The authors declare no competing financial interest.

■ REFERENCES

(1) Yang, W.-Q.; Liu, H.-G.; Gao, M.; Bai, Y.; Zhao, J.-T.; Xu, X.-D.; Wu, B.; Zheng, W.-C.; Liu, G.-K.; Lin, Y. Dual-Luminescence-Center Single-Component White-Light $Sr_2V_2O_7$:Eu^{3+} Phosphors for White LEDs. *Acta Mater.* **2013**, *61*, 5096−5104.

(2) Wang, R.; Xu, J.; Chen, C. Luminescent Characteristics of $Sr_2B_2O_5$: Tb^{3+}, Li^+ Green Phosphor. *Mater. Lett.* 2012, 68, 307−309.

(3) Li, P.; Xu, Z.; Zhao, S.; Zhang, F.; Wang, Y. Luminescent Characteristics and Energy Transfer of Ca_2BO_3Cl:Sm^{3+}, Eu^{3+} Red Phosphor. *Mater. Res. Bull.* 2012, 47, 3825−3829.

(4) Li, J.; Qiu, K.; Li, J.; Li, W.; Yang, Q.; Li, J. A Novel Broadband Emission Phosphor $Ca_2KMg_2V_3O_{12}$ for White Light Emitting Diodes. *Mater. Res. Bull.* 2010, 45, 598−602.

(5) Kuang, S.-P.; Meng, Y.; Liu, J.; Wu, Z.-C.; Zhao, L.-S. A New Self-Activated Yellow-Emitting Phosphor $Zn_2V_2O_7$ for White LED. *Optik* 2013, 124, 5517−5519.

(6) Zhao, L. S.; Liu, J.; Wu, Z. C.; Kuang, S. P. Optimized Photoluminescence of SrB_2O_4:Eu^{3+} Red-Emitting Phosphor by Charge Compensation. *Spectrochim. Acta, Part A* 2012, 87, 228−31.

(7) Guo, N.; Huang, Y.; Yang, M.; Song, Y.; Zheng, Y.; You, H. A Tunable Single-Component Warm White-Light $Sr_3Y(PO_4)_3$:Eu^{2+}, Mn^{2+} Phosphor for White-Light Emitting Diodes. *Phys. Chem. Chem. Phys.* 2011, 13, 15077−82.

(8) Zhou, J.; Huang, F.; Xu, J.; Chen, H.; Wang, Y. Luminescence Study of a Self-Activated and Rare Earth Activated $Sr_3La(VO_4)_3$ Phosphor Potentially Applicable in W-LEDs. *J. Mater. Chem. C* 2015, 3, 3023−3028.

(9) Nakajima, T.; Isobe, M.; Tsuchiya, T.; Ueda, Y.; Manabe, T. Photoluminescence Property of Vanadates $M_2V_2O_7$ (M: Ba, Sr and Ca). *Opt. Mater.* 2010, 32, 1618−1621.

(10) Nakajima, T.; Isobe, M.; Tsuchiya, T.; Ueda, Y.; Kumagai, T. A Revisit of Photoluminescence Property for Vanadate Oxides AVO_3 (A:K, Rb and Cs) and $M_3V_2O_8$ (M:Mg and Zn). *J. Lumin.* 2009, 129, 1598−1601.

(11) Pu, Y.; Huang, Y.; Tsuboi, T.; Huang, W.; Chen, C.; Seo, H. J. An Efficient Yellow-Emitting Vanadate $Cs_5V_3O_{10}$ under UV Light and X-Ray Excitation. *Mater. Lett.* 2015, 149, 89−91.

(12) Min, X.; Huang, Z.; Fang, M.; Liu, Y.; Tang, C.; Wu, X. Luminescence Properties of Self-Activated $Mm(VO_4)_2$ (M = Mg, Ca, Sr, and Ba) Phosphors Synthesized by Solid-State Reaction Method. *J. Nanosci. Nanotechnol.* 2016, 16, 3684−9.

(13) Huang, Y.; Yu, Y. M.; Tsuboi, T.; Seo, H. J. Novel Yellow-Emitting Phosphors of $Ca_5M_4(VO_4)_6$ (M = Mg, Zn) with Isolated VO_4 Tetrahedra. *Opt. Express* 2012, 20, 4360−4368.

(14) Li, L.; Wang, W.; Pan, Y.; Zhu, Y.; Liu, X.; Noh, H. M.; Moon, B. K.; Choi, B. C.; Jeong, J. H. Preferential Occupancy of Eu^{3+} and Energy Transfer in Eu^{3+} Doped $Sr_2V_2O_7$, $Sr_9Gd(VO_4)_7$ and $Sr_2V_2O_7$/$Sr_9Gd(VO_4)_7$ Phosphors. *RSC Adv.* 2018, 8, 1191−1202.

(15) Mi, L.; Huang, Y.; Liu, X.; Qin, L.; Seo, H. J. Improvement of Self-Activated Luminescence from Introduced Cation Disorder in $Sr_6V_2O_{11}$. *J. Am. Ceram. Soc.* 2018, 101, 2987−2995.

(16) Gupta, S. K.; Sudarshan, K.; Kadam, R. M. Tunable White Light Emitting $Sr_2V_2O_7$:Bi^{3+} Phosphors: Role of Bismuth Ion. *Mater. Des.* 2017, 130, 208−214.

(17) Matsushima, Y.; Koide, T.; Hiro-Oka, M.; Shida, M.; Sato, A.; Sugiyama, S.; Ito, M.; McKittrick, J. Self-Activated Vanadate Compounds Toward Realization of Rare-Earth-Free Full-Color Phosphors. *J. Am. Ceram. Soc.* 2015, 98, 1236−1244.

(18) Sharma, A.; Varshney, M.; Chae, K.-H.; Won, S. O. Electronic Structure and Luminescence Assets in White-Light Emitting $Ca_2V_2O_7$, $Sr_2V_2O_7$ and $Ba_2V_2O_7$ Pyro-Vanadates: X-Ray Absorption Spectroscopy Investigations. *RSC Adv.* 2018, 8, 26423−26431.

(19) Lim, C. S.; Atuchin, V. V. Preparation and Characterization of $Sr_3V_2O_8$ Nanoparticles Performed Via Cyclic MAS Route. *Metamaterials VIII: Proceedings*; SPIE: Prague, Czech Republic, 2013; Vol. 8771, p 877112.

(20) Zhu, W. L.; Ma, Y. Q.; Zhai, C.; Yang, K.; Zhang, X.; Wu, D. D.; Li, G.; Zheng, G. H. Photoluminescence Properties of $Sr_3(VO_4)_2$, $Sr_2Y_{2/3-Y}Eu_y(VO_4)_2$ and $Sr_2Y_{2/3-Z}Sm_z(VO_4)_2$. *Opt. Mater.* 2011, 33, 1162−1166.

(21) Alain, M.; Jacques, M.; Diane, M.-B.; Karine, P. Max: Multiplatform Applications for XAFS. *J. Phys.: Conf. Ser.* 2009, 190, 012034.

(22) Dovesi, R.; Orlando, R.; Erba, A.; Zicovich-Wilson, C. M.; Civalleri, B.; Casassa, S.; Maschio, L.; Ferrabone, M.; De La Pierre, M.; et al. CRYSTAL14: A Program for the Ab Initio Investigation of Crystalline Solids. *Int. J. Quantum Chem.* 2014, 114, 1287−1317.

(23) Becke, A. D. Density-Functional Thermochemistry. III. The Role of Exact Exchange. *J. Chem. Phys.* 1993, 98, 5648−5652.

(24) Lee, C.; Yang, W.; Parr, R. G. Development of the Colle-Salvetti Correlation-Energy Formula into a Functional of the Electron Density. *Phys. Rev. B: Condens. Matter Mater. Phys.* 1988, 37, 785−789.

(25) Teixeira, M. M.; de Oliveira, R. C.; Oliveira, M. C.; Pontes Ribeiro, R. A.; de Lazaro, S. R.; Li, M. S.; Chiquito, A. J.; Gracia, L.; Andres, J.; Longo, E. Computational Chemistry Meets Experiments for Explaining the Geometry, Electronic Structure, and Optical Properties of $Ca_{10}V_6O_{25}$. *Inorg. Chem.* 2018, 57, 15489−15499.

(26) Arumugam, D.; et al. Growth Mechanism of Pine-Leaf-Like Nanostructure from the Backbone of $SrCO_3$ Nanorods Using Lamer's Surface Diffusion: Impact of Higher Surface Energy (γ = 38.9 eV/nm^2) {111} Plane Stacking Along ⟨110⟩ (γ = 3.4 eV/nm^2) by First-Principles Calculations. *Cryst. Growth Des.* 2017, 17, 6394−6406.

(27) Thongtem, T.; Tipcompor, N.; Phuruangrat, A.; Thongtem, S. Characterization of $SrCO_3$ and $BaCO_3$ Nanoparticles Synthesized by Sonochemical Method. *Mater. Lett.* 2010, 64, 510−512.

(28) Cavalcante, L. S.; Longo, V. M.; Sczancoski, J. C.; Almeida, M. A. P.; Batista, A. A.; Varela, J. A.; Orlandi, M. O.; Longo, E.; Li, M. S. Electronic Structure, Growth Mechanism and Photoluminescence of $CaWO_4$ crystals. *CrystEngComm* 2012, 14, 853−868.

(29) Menezes, W. G.; Reis, D. M.; Oliveira, M. M.; Soares, J. F.; Zarbin, A. J. G. Vanadium Oxide Nanostructures Derived from a Novel Vanadium(IV) Alkoxide Precursor. *Chem. Phys. Lett.* 2007, 445, 293−296.

(30) Liu, G.; Duan, X.; Li, H.; Dong, H. Hydrothermal Synthesis, Characterization and Optical Properties of Novel Fishbone-Like $LaVO_4$:Eu^{3+} Nanocrystals. *Mater. Chem. Phys.* 2009, 115, 165−171.

(31) Zhang, M.; Maddrell, E. R.; Abraitis, P. K.; Salje, E. K. H. Impact of Leach on Lead Vanado-Iodoapatite $[Pb_5(VO_4)_3I]$: An Infrared and Raman Spectroscopic Study. *Mater. Sci. Eng., B* 2007, 137, 149−155.

(32) Slobodin, B. V., et al. Structural, Luminescence, and Electronic Properties of the Alkaline Metal-Strontium Cyclotetravanadates $M_2Sr(VO_3)_4$, (M = Na, K, Rb, Cs). *Phys. Rev. B* 2005, 72.

(33) Sha, F.; Guo, B.; Zhang, F.; Yang, X.; Qiao, X.; Liu, C.; Zhao, B.; Zhang, J. Morphology Control of $SrCO_3$ Crystals on the Basis of a CO_2 Capture Utilization and Storage Strategy. *Chemistry Select* 2016, 1, 2652−2663.

(34) Raschetti, M.; Byzynski, G.; Ribeiro, C.; Longo, E. N-Doping $SrTiO_3$@$SrCO_3$ Heterostructure Electrode: Synthesis, Electrochemical Characterization, and Varistor Application. *Ceram. Int.* 2017, 43, 11722−11732.

(35) Stoch, J.; Gablankowska-Kukucz, J. The Effect of Carbonate Contaminations on the XPS-O-1s Band-Structure in Metal-Oxides. *Surf. Interface Anal.* 1991, 17, 165−167.

(36) Bourlier, Y.; Frégnaux, M.; Bérini, B.; Fouchet, A.; Dumont, Y.; Aureau, D. Surface Characterizations and Selective Etching of Sr-Rich Segregation on Top of $SrVO_3$ Thin-Films Grown by Pulsed Laser Deposition. *ChemNanoMat* 2019, 5, 674−681.

(37) Silversmit, G.; Depla, D.; Poelman, H.; Marin, G. B.; De Gryse, R. Determination of the V2p XPS Binding Energies for Different Vanadium Oxidation States (V^{5+} to V^{0+}). *J. Electron Spectrosc. Relat. Phenom.* 2004, 135, 167−175.

(38) Sarin, N.; Mishra, M.; Gupta, G.; Arora, M.; Luthra, V. Deciphering the Role of Oxygen Vacancies on Structural, Electrical, and Magnetic Properties of Fe-Substituted Strontium Titanate. *Phys. Status Solidi B* 2018, 255, 1700683.

(39) Han, Z.; Yang, Y.; Kong, D. Surface-Scale Affinity and Adsorption Selectivity of Alkaline Earth Metal Oxides to H_2O and CO_2: Insight into SOFC Anode Modification. *Appl. Surf. Sci.* 2020, 503, 144333.

(40) Hong, J.; Heo, S. J.; Aphale, A. N.; Hu, B.; Singh, P. H_2O Absorption Assisted Sr-Segregation in Strontium Nickel Oxide Based

Chromium Getter and Encapsulation with SrCO$_3$. *J. Electrochem. Soc.* **2019**, *166*, F59−F65.

(41) Duan, Y.; Sorescu, D. C. CO$_2$ Capture Properties of Alkaline Earth Metal Oxides and Hydroxides: A Combined Density Functional Theory and Lattice Phonon Dynamics Study. *J. Chem. Phys.* **2010**, *133*, 074508.

(42) Darvishnejad, M. H.; Reisi-Vanani, A. Multiple CO$_2$ Capture in Pristine and Sr-Decorated Graphyne: A DFT-D3 and AIMD Study. *Comput. Mater. Sci.* **2020**, *176*, 109539.

(43) Unnimaya, A. N.; Suresh, E. K.; Ratheesh, R. Crystal Structure and Microwave Dielectric Properties of New Alkaline Earth Vanadate A$_4$V$_2$O$_9$ (a = Ba, Sr, Ca, Mg and Zn) Ceramics for LTCC Applications. *Mater. Res. Bull.* **2017**, *88*, 174−181.

(44) Souza, A. E.; Santos, G. T. A.; Barra, B. C.; Macedo, W. D.; Teixeira, S. R.; Santos, C. M.; Senos, A. M. O. R.; Amaral, L.; Longo, E. Photoluminescence of SrTiO$_3$: Influence of Particle Size and Morphology. *Cryst. Growth Des.* **2012**, *12*, 5671−5679.

(45) Ni, S.; Yang, X.; Li, T. Hydrothermal Synthesis and Photoluminescence Properties of SrCO$_3$. *Mater. Lett.* **2011**, *65*, 766−768.

(46) Chaurand, P.; Rose, J.; Briois, V.; Salome, M.; Proux, O.; Nassif, V.; Olivi, L.; Susini, J.; Hazemann, J.-L.; Bottero, J.-Y. New Methodological Approach for the Vanadium K-edge X-Ray Absorption near-Edge Structure Interpretation: Application to the Speciation of Vanadium in Oxide Phases from Steel Slag. *J. Phys. Chem. B* **2007**, *111*, 5101−5110.

(47) Lu, Y.-R.; Hsu, H.-H.; Chen, J.-L.; Chang, H.-W.; Chen, C.-L.; Chou, W.-C.; Dong, C.-L. Atomic and Electronic Aspects of the Coloration Mechanism of Gasochromic Pt/Mo-Modified V$_2$O$_5$ Smart Films: An in Situ X-Ray Spectroscopic Study. *Phys. Chem. Chem. Phys.* **2016**, *18*, 5203−5210.

(48) Marques, M. P. M.; Gianolio, D.; Ramos, S.; Batista de Carvalho, L. A. E.; Aureliano, M. An EXAFS Approach to the Study of Polyoxometalate-Protein Interactions: The Case of Decavanadate-Actin. *Inorg. Chem.* **2017**, *56*, 10893−10903.

(49) Avansi, W., Jr.; Ribeiro, C.; Leite, E. R.; Mastelaro, V. R. Vanadium Pentoxide Nanostructures: An Effective Control of Morphology and Crystal Structure in Hydrothermal Conditions. *Cryst. Growth Des.* **2009**, *9*, 3626−3631.

(50) Mansour, A. N.; Smith, P. H.; Balasubramanian, M.; McBreen, J. In Situ X-Ray Absorption Study of Cycled Ambigel V$_2$O$_5$·nH$_2$O-($n \approx 0.5$) Composite Cathodes. *J. Electrochem. Soc.* **2005**, *152*, A1312.

(51) Sharma, A.; Varshney, M.; Cheol Lim, W.; Shin, H. J.; Pal Singh, J.; Ok Won, S.; Hwa Chae, K. Mechanistic Insights on the Electronic Properties and Electronic/Atomic Structure Aspects in Orthorhombic SrVO$_3$ Thin Films: XANES-EXAFS Study. *Phys. Chem. Chem. Phys.* **2017**, *19*, 6397−6405.

(52) Wu, Y.; Fan, L.; Huang, W.; Chen, S.; Chen, S.; Chen, F.; Zou, C.; Wu, Z. Depressed Transition Temperature of W$_X$V$_{1-X}$O$_2$: Mechanistic Insights from the X-Ray Absorption Fine Structure (XAFS) Spectroscopy. *Phys. Chem. Chem. Phys.* **2014**, *16*, 17705−14.

(53) Ronde, H.; Blasse, G. The Nature of the Electronic Transitions of the Vanadate Group. *J. Inorg. Nucl. Chem.* **1978**, *40*, 215−219.

(54) Xu, J.; Hu, C.; Xi, Y.; Peng, C.; Wan, B.; He, X. Synthesis, Photoluminescence and Magnetic Properties of Barium Vanadate Nanoflowers. *Mater. Res. Bull.* **2011**, *46*, 946−950.

(55) Nakajima, T.; Isobe, M.; Tsuchiya, T.; Ueda, Y.; Manabe, T. Correlation between Luminescence Quantum Efficiency and Structural Properties of Vanadate Phosphors with Chained, Dimerized, and Isolated VO$_4$ Tetrahedra. *J. Phys. Chem. C* **2010**, *114*, 5160−5167.

(56) Dutta, D. P.; Ghildiyal, R.; Tyagi, A. K. Luminescent Properties of Doped Zinc Aluminate and Zinc Gallate White Light Emitting Nanophosphors Prepared Via Sonochemical Method. *J. Phys. Chem. C* **2009**, *113*, 16954−16961.

(57) Sindhu, H. S.; Rajendra, B. V.; Hebbar, N. D.; Kulkarni, S. D.; Babu, P. D. Defect Induced White-Light Emission from Mn-Doped Zno Films and Its Magnetic Properties. *J. Lumin.* **2018**, *199*, 423−432.